metals

MDPI

Article

Integrated Pyrometallurgical Recovery of High-Purity Fe from Spent $LiFePO_4$ Batteries Through Selective Cu Removal and Oxidative Dephosphorization

A-Jin Im and Jei-Pil Wang *

BB21 Plus Team, Department of Metallurgical Engineering, Pukyong National University, Busan 48513, Republic of Korea

* Correspondence: jpwang@pknu.ac.kr

Abstract

Spent lithium iron phosphate ($LiFePO_4$, LFP) batteries contain considerable amounts of Fe; however, most conventional recycling processes primarily target Li recovery, while Fe is often discarded or utilized as a low-value residue. In this study, an integrated pyrometallurgical refining process was developed to recover and purify Fe from spent LFP battery-derived materials through sequential Cu and P removal. Following decarbonization and oxidative smelting, an FeO-rich slag was subjected to carbothermic reduction to produce an Fe–Cu–P alloy. Cu was subsequently removed by FeS-assisted sulfidation and slag refining, and the remaining P was removed by oxidative dephosphorization using Fe_2O_3 and a $CaO–SiO_2$-based slag. The effects of reaction temperature, Cu molar ratio, and slag basicity were systematically investigated. The optimum Cu-removal condition was obtained at 1400 °C with a Cu molar ratio of 2:1, under which the Cu content decreased from 6.44 to 1.47 wt.%, corresponding to an estimated Cu-removal efficiency of 77.45%. Subsequent dephosphorization was strongly influenced by slag basicity. Increasing the CaO/SiO_2 ratio from 2.0 to 3.0 decreased the residual P content from 1.33 to 0.042 wt.% and increased the phosphorus distribution ratio from 3.36 to 138.57. At a basicity of 3.0, the P removal efficiency reached 99.44%. Under the optimum conditions, the final metallic product exhibited a calculated Fe purity of 98.55% with an Fe recovery of 93.27%. The results demonstrate that sequential sulfidation and oxidative dephosphorization can effectively remove Cu and P while minimizing Fe loss, providing a feasible pyrometallurgical route for upgrading Fe recovered from spent LFP batteries into a reusable metallic resource.

Keywords: spent $LiFePO_4$ battery; pyrometallurgical recycling; iron recovery; selective Cu removal; sulfidation; dephosphorization; slag basicity; Fe_2O_3; $CaO–SiO_2$ slag

Check for updates

Academic Editor: Srecko Stopic

Received: 24 August 2026
Revised: 14 September 2026
Accepted: 16 September 2026
Published: 18 September 2026

Copyright: © 2026 by the authors. Licensee MDPI, Basel, Switzerland. This article is an open access article distributed under the terms and conditions of the Creative Commons Attribution (CC BY) license.

1. Introduction

Lithium-ion batteries (LIBs) have become indispensable energy-storage devices for portable electronics, electric vehicles (EVs), and energy storage systems (ESSs) because of their high energy density, long cycle life, high operating efficiency, and favorable electrochemical performance [1,2]. The rapid expansion of EV and large-scale ESS applications has consequently increased the global demand for LIBs, while simultaneously accelerating the generation of spent batteries [3]. This trend has intensified the need for efficient recycling technologies capable of recovering valuable resources and reducing the environmental burden associated with end-of-life batteries.

Improper disposal of spent LIBs can result in the loss of valuable metal resources and may cause environmental contamination. In addition, the increasing demand for battery raw materials has raised concerns regarding resource security, energy consumption, and the environmental impacts associated with primary extraction and refining [3,4]. Therefore, the development of sustainable recycling technologies is essential for establishing a circular battery-material supply chain.

Among the various LIB chemistries, lithium iron phosphate ($LiFePO_4$, LFP) batteries have attracted increasing attention because of their excellent thermal stability, long cycle life, relatively low cost, and absence of high-cost Co and Ni in the cathode material [5–8]. Their use has expanded rapidly, particularly in EV and ESS applications. Nevertheless, spent LFP batteries generally have a lower intrinsic recycling value than Ni–Co–Mn-based batteries because their principal metallic constituents are Li and Fe rather than high-value Co and Ni [5–8]. This economic limitation has stimulated increasing interest in processes capable of recovering not only Li but also Fe and P as useful secondary resources.

Various approaches have been investigated for recycling spent LFP batteries, including hydrometallurgical processing, pyrometallurgical treatment, direct regeneration, and combined recycling processes [5–9]. Among these approaches, hydrometallurgical processes have been extensively studied because they can achieve selective Li extraction and high recovery efficiencies under relatively mild temperature conditions [9–11]. However, these processes often require acidic or alkaline reagents and multiple separation and purification steps. Moreover, many LFP recycling processes focus primarily on Li recovery, while Fe is retained as $FePO_4$, Fe-containing precipitates, or other solid residues rather than being recovered as a reusable metallic resource [9–11]. Consequently, improving the utilization of Fe represents an important opportunity for increasing the overall resource value of spent LFP batteries.

High-temperature processing provides an alternative route for treating heterogeneous battery materials because metallic and oxide phases can be separated directly without extensive aqueous purification. Recent work has further demonstrated that Fe, Li, and P can be separated and recovered from spent $LiFePO_4$ using high-temperature molten-salt processing, highlighting the potential value of Fe as a recoverable secondary resource rather than simply a low-value residue [12]. Nevertheless, Fe-rich metallic products recovered from spent LFP materials can contain residual Cu and P originating primarily from Cu current collectors and $LiFePO_4$ cathode materials, respectively.

These residual elements can significantly restrict the direct reuse of recovered Fe. Cu is a well-known residual element associated with surface hot-shortness and deterioration of hot workability during steel processing [13], whereas P segregation at ferrite grain boundaries can adversely affect grain-boundary properties and contribute to embrittlement of Fe-based materials [14]. Therefore, effective control of both Cu and P is required to upgrade recovered Fe to a reusable metallic product.

In our previous study, an Fe–P–Cu alloy recovered through pyrometallurgical reduction of spent $LiFePO_4$ batteries was subjected to FeS-assisted sulfidation and fayalite-slag refining [15]. The results demonstrate preferential transfer of Cu from the metallic phase to Cu–Fe–S sulfide phases, confirming the feasibility of selective Cu removal based on differences in sulfur affinity. However, a considerable amount of P remained in the refined metallic phase. Thus, Cu removal alone was insufficient to achieve high-purity Fe, and an additional dephosphorization step was required.

Oxidative dephosphorization is widely employed in Fe and steel refining to transfer phosphorus from the metallic phase to a basic oxide slag. Fe_2O_3 addition can increase the interfacial oxygen activity and enhance phosphorus oxidation and dephosphorization kinetics [16]. In addition, the distribution and stabilization of phosphorus in CaO–SiO_2–

FeO_x-based slags are strongly influenced by slag basicity and phase constitution [17]. Therefore, control of both oxidation potential and slag chemistry is critical for achieving deep dephosphorization while limiting Fe loss.

Recent recycling studies continue to emphasize selective Li recovery from spent LFP materials, including electrochemical processes capable of achieving high Li extraction while suppressing Fe dissolution [18]. Although such approaches are effective for Li recovery, comparatively little attention has been given to upgrading Fe recovered directly as a metallic resource through sequential impurity removal. In particular, an integrated process combining selective Cu removal and subsequent oxidative dephosphorization of an Fe-rich alloy derived from spent LFP batteries has rarely been investigated.

In the present study, an integrated pyrometallurgical process was investigated for the recovery and purification of Fe from spent LFP battery materials. The process consisted of the production of an Fe–Cu–P alloy, selective Cu removal through FeS-assisted sulfidation and slag refining, and subsequent oxidative dephosphorization using Fe_2O_3 and a $CaO–SiO_2$-based slag. The novelty of the present study lies in integrating these sequential Cu- and P-removal steps into a single Fe-upgrading route for spent LFP-derived materials, thereby extending our previous Cu-removal study [15] to the subsequent deep dephosphorization and overall evaluation of the recovered Fe-rich metallic product. Unlike studies focused primarily on Li recovery or on a single impurity-removal stage, this work evaluates the combined control of Cu and P through sequential sulfidation and oxidative slag refining. The effects of reaction temperature and FeS addition on Cu removal were evaluated, while the influence of slag basicity on phosphorus distribution, P removal efficiency, calculated Fe content, and estimated Fe recovery was systematically investigated. The feasibility of the sequential Cu- and P-removal process was assessed based on the final impurity concentrations and Fe recovery.

2. Materials and Methods

2.1. Feed Material and Characterization

Shredded materials obtained from spent $LiFePO_4$ (LFP) batteries were supplied by a recycling company in Korea and used as the initial feed material. The heterogeneous feed consisted of cathode and anode active materials, current-collector fragments, and other battery-derived components, as shown in Figure 1.

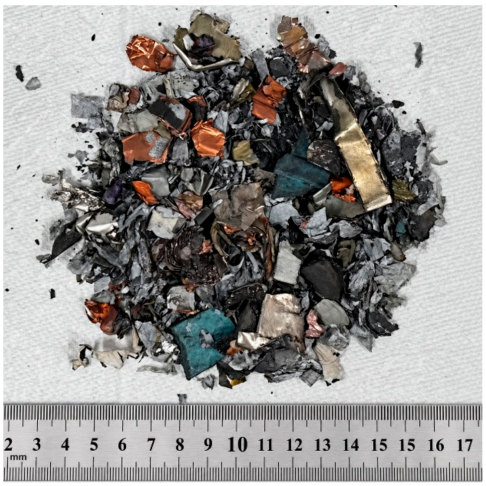


Figure 1. Photograph of the shredded materials obtained from spent LFP batteries.

Prior to chemical characterization, the shredded material was sieved using a stainless-steel mesh test sieve with a 4 mm aperture (RETSCH GmbH, Haan, Germany). The

crystalline phases were identified by X-ray diffraction (XRD; D8 DISCOVER, Bruker AXS, Karlsruhe, Germany), while the elemental composition was analyzed using inductively coupled plasma–optical emission spectrometry (ICP–OES; Optima 8300, PerkinElmer, Waltham, MA, USA) and a carbon/sulfur analyzer. The XRD pattern and the measured Li and C contents are presented in Figure 2 and Table 1, respectively. Table 1 presents only the Li and C contents relevant to the present process design and does not represent a complete elemental inventory of the shredded feed. The remaining fraction consisted primarily of other battery-derived inorganic constituents, including Fe-, P-, and Cu-containing components, together with minor Al, Ni, S, Co, Cr, and Si, as subsequently identified in the decarbonized product.

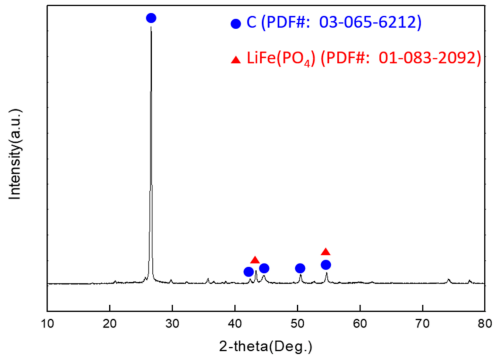


Figure 2. XRD pattern of the shredded spent LFP battery material. The identified phases correspond to graphite and $LiFePO_4$.

Table 1. Selected Li and C contents of the shredded spent LFP battery material determined by ICP–OES and C/S analysis.

Element	Content (wt.%)
Li	0.67
C	29.1

The XRD pattern showed a strong diffraction peak attributed to graphite, together with several peaks corresponding to residual $LiFePO_4$. The carbon content of the shredded material was 29.1 wt.%, which was mainly attributed to graphite originating from the anode material and conductive carbon additives. Because this carbon could act as a reductant for Fe-containing oxides during subsequent high-temperature treatment, its presence could significantly affect slag formation, reduction behavior, and metal recovery. Therefore, a controlled decarbonization pretreatment was conducted before the pyrometallurgical refining experiments.

2.2. Decarbonization Pretreatment

The carbon-rich shredded material was subjected to oxidative heat treatment in an atmosphere-controlled electric furnace. Thermodynamic calculations performed using HSC Chemistry 6, version 6.12 (Outotec Research Oy, Pori, Finland) indicated that carbon oxidation was thermodynamically favorable at 800 °C. The carbon oxidation reaction was initially considered as follows:

$$2C + O_2 \rightarrow 2CO \quad (1)$$

$$C(s) + O_2 \rightarrow CO_2(g) \quad (2)$$

The calculated standard Gibbs energy change for Reaction (1) at 800 °C was −98.820 kcal mol^{-1}. To determine an appropriate oxygen supply, decarbonization experiments were performed at oxygen-equivalent ratios of 1.0, 1.5, and 2.1 relative to the

initial carbon content of the feed. The residual carbon contents after oxidative treatment are listed in Table 2.

Table 2. Effect of the oxygen-equivalent ratio on the residual carbon content after oxidative treatment at 800 °C for 2 h.

Condition	Oxygen-Equivalent Ratio	Residual C Content (wt.%)
1	1.0	8.232
2	1.5	3.651
3	2.1	0.190

Increasing the oxygen-equivalent ratio markedly decreased the residual carbon content. At oxygen-equivalent ratios of 1.0 and 1.5, the residual carbon contents were 8.232 and 3.651 wt.%, respectively. When the oxygen-equivalent ratio was increased to 2.1, the residual carbon content decreased to 0.190 wt.%. An oxygen-equivalent ratio of 2.1 was therefore selected for the decarbonization pretreatment. A further increase in oxygen supply was avoided to minimize the oxidation of Fe-containing components. After treatment at an oxygen-equivalent ratio of 2.1, 52 g of solid product was recovered from the initial 100 g of feed. The recovered product was analyzed by X-ray fluorescence spectroscopy, and the results are shown in Table 3. The product contained 42.25 wt.% Cu, 39.52 wt.% Fe, and 13.03 wt.% P as its major constituents. The decarbonized material was subsequently used as the feed for the pyrometallurgical alloy-production experiments.

Table 3. Chemical composition of the recovered product after decarbonization at an oxygen-equivalent ratio of 2.1.

Element	Content (wt.%)
Cu	42.25
Fe	39.52
P	13.03
Al	2.84
Ni	0.89
S	0.55
Co	0.35
Cr	0.26
Si	0.24

2.3. Experimental Apparatus

The pyrometallurgical experiments were conducted using laboratory-scale furnaces capable of high-temperature operation under controlled gas atmospheres. A vertical tube furnace with a maximum operating temperature of approximately 1700 °C was primarily used for alloy production, premelted-slag preparation, Cu removal, and dephosphorization experiments. The furnace was equipped with Kanthal heating elements and an alumina reaction tube. The reaction temperature was measured and controlled using a Type C thermocouple composed of W–5 wt.% Re and W–26 wt.% Re wires. The thermocouple was positioned adjacent to the crucible to monitor the temperature of the reaction zone. The crucible was placed at the center of the uniform-temperature zone and supported by refractory materials during high-temperature treatment. A schematic diagram of the vertical tube furnace is presented in Figure 3.

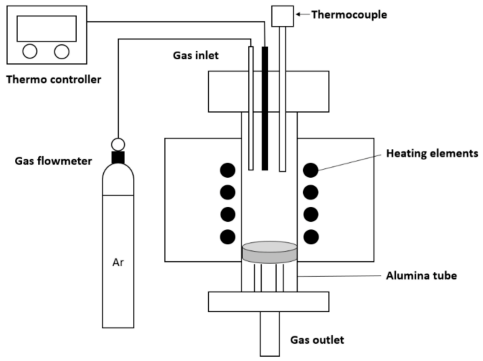


Figure 3. Schematic illustration of the vertical tube furnace used for the high-temperature refining experiments.

Some melting and reduction experiments were conducted using a high-frequency induction furnace to achieve rapid heating and complete melting of the charge. The specific furnace used for each experimental stage and the corresponding operating conditions are described in the relevant subsections. Two types of crucibles were employed depending on the experimental purpose. Alumina crucibles with an inner diameter of approximately 4.4 cm and a height of 6.0 cm were used for Fe-based alloy production. MgO crucibles with an inner diameter of approximately 5.0 cm and a height of 9.0 cm were used for premelted-slag preparation and dephosphorization experiments to minimize reactions between the CaO-containing slag and the crucible material. During dephosphorization, the MgO crucible was additionally placed inside an outer graphite crucible to improve mechanical stability and protect the reaction crucible at high temperatures.

The experiments were performed under controlled Ar, CO–CO_2, or O_2-containing atmospheres, depending on the purpose of each experimental stage. Before heating, the reaction tube was purged with Ar to remove residual air. The process gas was introduced from the upper part of the reaction tube and discharged through the lower outlet. The gas flow rates were regulated using flowmeters. CO–CO_2 gas mixtures were used when control of the equilibrium oxygen partial pressure was required, whereas O_2 was supplied during oxidative treatment. The reaction temperature was continuously monitored, and the samples were maintained at the target temperature for the prescribed reaction time. The crystalline phases and chemical compositions of the feed materials and reaction products were characterized using X-ray diffraction (XRD), inductively coupled plasma–optical emission spectrometry (ICP–OES), scanning electron microscopy coupled with energy-dispersive X-ray spectroscopy (SEM–EDS) (Bruker Nano GmbH, Berlin, Germany), and X-ray fluorescence spectroscopy (XRF). Carbon and sulfur contents were determined using an ELEMENTRAC CS-i carbon/sulfur analyzer (ELTRA GmbH, Haan, Germany).

2.4. Overall Experimental Procedure

The overall pyrometallurgical process employed in this study is illustrated in Figure 4. The shredded spent LFP battery material was first subjected to decarbonization to remove residual graphite and conductive carbon. The decarbonized feed was then treated by oxidative smelting at 1350 °C for 10 h under a controlled CO–CO_2 atmosphere to separate a dense Cu-rich metallic/speiss-like phase from an FeO-rich slag. During this stage, Li was associated primarily with the oxide slag stream rather than with the Cu-rich speiss phase. Because Li recovery was not the focus of the present study, its distribution in the subsequent slag products was not quantitatively determined. Residual Li is therefore expected to remain predominantly in the oxide/slag fractions generated during the subsequent pyrometallurgical treatments rather than in the recovered Fe-rich metallic product. Subsequently, the FeO-rich slag was subjected to carbothermic reduction in the presence of

carbon and CaO flux, resulting in the formation of an Fe–Cu–P alloy and a P-containing primary slag. The resulting Fe–Cu–P alloy was further refined through FeS-assisted sulfidation using an Fe_2SiO_4-based flux. During this stage, Cu removal from the metallic phase was promoted through preferential sulfidation, producing a Cu-depleted Fe–P alloy. The Fe–P alloy was then subjected to oxidative dephosphorization using Fe_2O_3 as the oxidizing agent and a CaO–SiO_2-based slag. Oxidized phosphorus was transferred to a P-containing secondary slag, while the Fe-rich metallic product remained in the metallic phase. Accordingly, the integrated process combined oxidative phase separation, carbothermic reduction, selective sulfidation, and oxidative slag refining to sequentially remove Cu and P from the Fe-bearing material derived from spent LFP batteries. A quantitative evaluation of Li distribution and recovery throughout the integrated process remains an important subject for future work.

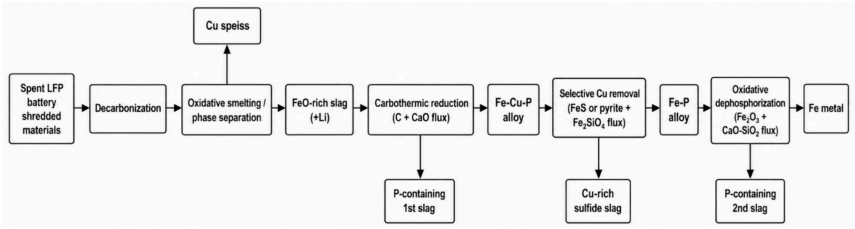


Figure 4. Schematic flow diagram of the integrated pyrometallurgical process for recovering purified Fe from spent LFP battery materials.

2.5. Production of the Fe–Cu–P Alloy

2.5.1. Oxidative Smelting and Phase Separation

The decarbonized spent LFP battery material was subjected to oxidative smelting to separate a Cu-rich metallic/speiss-like phase from an FeO-rich slag. Here, the term "speiss-like phase" denotes the dense Cu-rich metallic phase formed during oxidative smelting and physically separated from the lower-density oxide slag. The oxygen potential required to maintain Fe predominantly in the FeO-containing slag phase was evaluated using thermodynamic calculations.

The Fe/FeO and FeO/Fe_3O_4 equilibria were considered according to the following reactions:

$$2Fe(\mathrm{l}) + O_2 \rightarrow 2FeO(\mathrm{l}) \quad (3)$$

$$3FeO(\mathrm{l}) + \frac{1}{2}O_2(\mathrm{g}) \rightarrow Fe_3O_4(\mathrm{s}) \quad (4)$$

The Gibbs energy change for Reaction (3), calculated using HSC Chemistry, was:

$$\Delta G^{\circ}_{1600\ ^{\circ}\mathrm{C}} = -289.399\ \mathrm{kJ\ mol^{-1}}$$

The Gibbs energy change for the formation of Fe_3O_4 from metallic Fe was also calculated using:

$$3Fe(\mathrm{l}) + 2O_2(\mathrm{g}) \rightarrow Fe_3O_4(\mathrm{s}) \quad (5)$$

$$\Delta G^{\circ}_{1600\ ^{\circ}\mathrm{C}} = -528.318\ \mathrm{kJ\ mol^{-1}}$$

Based on the calculated Fe–O equilibria, the oxygen partial pressure was controlled to suppress the reduction of FeO to metallic Fe while avoiding excessive oxidation of FeO to Fe_3O_4. The decarbonized product (52 g) was mixed with 11.05 g of SiO_2 and charged into an alumina crucible. The sample was heated at 1350 °C for 10 h under a CO–CO_2 gas atmosphere corresponding to an equilibrium oxygen partial pressure of approximately 10^{-11} atm. Under the controlled oxygen potential, Fe was preferentially oxidized to FeO and incorporated into an FeO–SiO_2–P-containing oxide slag, whereas Cu was preferentially

concentrated in a dense Cu-rich metallic/speiss-like phase. Because the metallic and oxide phases were mutually immiscible under the smelting conditions, clear macroscopic phase separation occurred. After cooling and removal from the crucible, the two solidified phases were sufficiently distinct to be manually separated without the use of special separation equipment. The separated phases were subsequently weighed, and the FeO-rich slag was subjected to XRD and XRF analyses. The XRD pattern of the recovered FeO-rich slag is presented in Figure 5, and its oxide-equivalent composition determined by XRF is summarized in Table 4. The XRD analysis confirmed the presence of crystalline phases containing FeO, SiO_2, phosphate species, and Cu, while the XRF analysis showed that FeO, P_2O_5, and SiO_2 were the principal components of the slag.

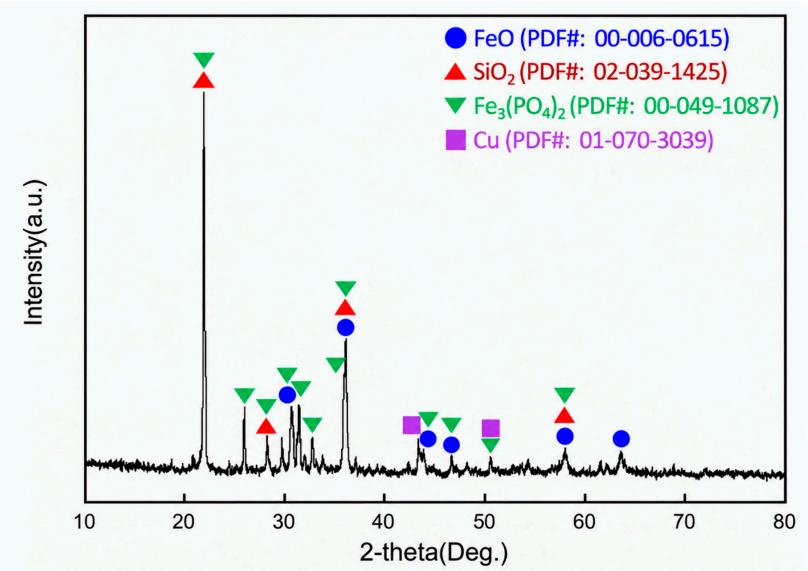


Figure 5. XRD pattern of the FeO-rich slag obtained after oxidative smelting and phase separation.

Table 4. Oxide-equivalent composition of the FeO-rich slag determined by XRF.

Component	Content (wt.%)
FeO	43.10
P_2O_5	26.70
SiO_2	23.56
CuO	4.61
S or SO_3	1.23
CoO	0.80

2.5.2. Thermodynamic Assessment of the FeO-Rich Slag

The melting behavior of the FeO-rich slag was evaluated using the FeO–SiO_2–P_2O_5 liquidus projection calculated with FactSage 8.2. The analyzed slag composition was renormalized based on the three principal components, FeO, SiO_2, and P_2O_5, before comparison with the calculated ternary system. The corresponding normalized composition was approximately 46.16 wt.% FeO, 25.24 wt.% SiO_2, and 28.60 wt.% P_2O_5. Figure 6 presents the simplified liquidus projection of the FeO–SiO_2–P_2O_5 system at 1 atm, with the normalized experimental slag composition indicated directly on the ternary diagram. The diagram shows the phase fields and liquidus-temperature contours over the ternary composition range. The position of the normalized experimental slag composition indicates that the FeO-rich slag lies in a relatively high-liquidus-temperature region. Therefore, a high treatment temperature was required to promote sufficient slag melting and effective metal–slag separation. Based on this thermodynamic assessment, together with the modification

of the slag composition through CaO addition, the subsequent carbothermic-reduction experiment was conducted at 1600 °C.

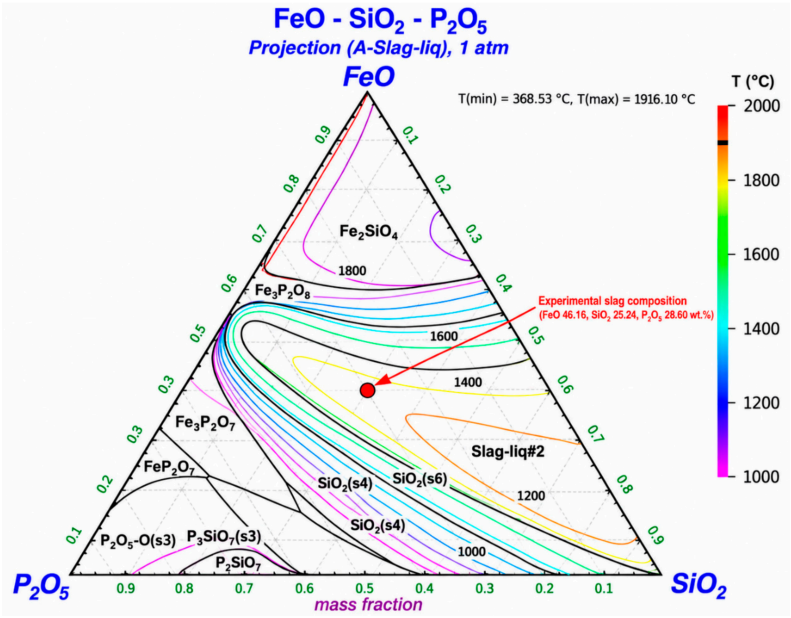


Figure 6. Calculated liquidus projection of the FeO–SiO_2–P_2O_5 system at 1 atm obtained using FactSage 8.2. The normalized experimental slag composition is indicated in the ternary diagram.

2.5.3. Carbothermic Reduction of the FeO-Rich Slag

The FeO-rich slag was subjected to carbothermic reduction to produce an Fe-based alloy. Graphite was used as the reducing agent, and CaO was added to modify the slag composition and stabilize phosphorus-containing oxide species.

The reduction of FeO was represented by:

$$FeO(\mathrm{l}) + C(\mathrm{s}) \rightarrow Fe(\mathrm{l}) + CO(\mathrm{g}) \quad (6)$$

The possible reduction of P_2O_5 was assessed using the following balanced reaction:

$$P_2O_5(\mathrm{l}) + 5C(\mathrm{s}) \rightarrow 2P(\mathrm{g}) + 5CO(\mathrm{g}) \quad (7)$$

In Reaction (7), elemental phosphorus was considered in the gaseous state for the standard-state thermodynamic calculation. Under the actual carbothermic-reduction conditions, however, part of the reduced phosphorus may dissolve into the Fe-rich metallic phase.

The Gibbs energy change calculated using HSC Chemistry was:

$$\Delta G^{\circ}_{1600\ ^{\circ}\mathrm{C}} = -698.732\ \mathrm{kJ\ mol^{-1}}$$

The reduction of CuO was represented by:

$$CuO(\mathrm{s}) + C(\mathrm{s}) \rightarrow Cu(\mathrm{l}) + CO(\mathrm{g}) \quad (8)$$

$$\Delta G^{\circ}_{1600\ ^{\circ}\mathrm{C}} = -272.441\ \mathrm{kJ\ mol^{-1}}$$

The reduction of $FePO_4$ in the presence of CaO was evaluated using the following balanced reaction:

$$2FePO_4(\mathrm{s}) + 2CaO(\mathrm{s}) + 3C(\mathrm{s}) \rightarrow 2Fe(\mathrm{l}) + Ca_2P_2O_7(\mathrm{s}) + 3CO(\mathrm{g}) \quad (9)$$

$$\Delta G^{\circ}_{1600\ ^{\circ}\mathrm{C}} = -1350.072\ \mathrm{kJ\ mol^{-1}}$$

The negative Gibbs energy values indicate that the reduction of Fe-containing oxides and phosphates was thermodynamically favorable under the selected conditions. However, the reduction of P_2O_5 may promote the transfer of P from the slag into the metallic phase. CaO was therefore added to stabilize phosphorus in the slag as Ca–P–O compounds and to modify the slag melting behavior. For each reduction experiment, 20 g of the FeO-rich slag, 2 g of graphite, and 9.42 g of CaO were charged into a graphite crucible. The nominal slag basicity was defined as:

$$B = \frac{CaO}{SiO_2} \tag{10}$$

and was adjusted to 2.0.

The sample was treated at 1600 °C for 50 min in a high-frequency induction furnace under Ar flowing at 300 mL $\mathrm{min^{-1}}$. After cooling, the metallic and slag phases were separated, and their local chemical compositions were analyzed using SEM–EDS.

2.5.4. Preliminary Oxidative Refining of the Fe-Based Alloy

The Fe-based alloy produced by carbothermic reduction contained phosphorus in Fe–P phases. A preliminary oxygen-blowing treatment was therefore conducted to oxidize P and transfer it into a CaO–SiO_2-containing slag.

The oxidation of FeP to Fe_3P and P_2O_5 was evaluated using:

$$3FeP(\mathrm{s}) + \frac{5}{2}O_2(\mathrm{g}) \rightarrow Fe_3P(\mathrm{s}) + P_2O_5 \tag{11}$$

$$\Delta G^{\circ}_{1600\ ^{\circ}C} = -585.53\ \mathrm{kJ\ mol^{-1}}$$

Further oxidation of Fe_3P was represented by:

$$2Fe_3P(\mathrm{s}) + \frac{5}{2}O_2\ (\mathrm{g}) \rightarrow 6Fe(\mathrm{l}) + P_2O_5 \tag{12}$$

$$\Delta G^{\circ}_{1600\ ^{\circ}C} = -513.904\ \mathrm{kJ\ mol^{-1}}$$

Both reactions exhibited negative Gibbs energy changes, indicating that the oxidative removal of P from Fe–P phases was thermodynamically favorable at 1600 °C.

The overall oxidation of dissolved P may also be expressed more generally as: Here, $[P]_{\mathrm{Fe}}$ denotes phosphorus dissolved in the Fe-rich metallic phase, with Fe acting as the solvent phase.

$$2[P]_{Fe} + \frac{5}{2}O_2(\mathrm{g}) \rightarrow P_2O_5 \tag{13}$$

For the preliminary oxidative-refining experiment, 30 g of the Fe-based alloy was mixed with 6.6 g of CaO and 3.3 g of SiO_2 in an alumina crucible. The sample was heated to 1600 °C, after which O_2 was supplied at 300 mL $\mathrm{min^{-1}}$ for 10 min. The resulting metallic and slag phases were characterized using SEM–EDS.

2.6. Selective Cu Removal

The Fe–Cu–P alloy obtained from the preceding reduction and preliminary refining stages was subjected to selective Cu removal through FeS-assisted sulfidation and slag refining. FeS or pyrite was used as the sulfur source, while a Fe_2SiO_4-based flux was added to promote the separation of the metallic and sulfide-rich phases. Before the sulfidation experiments, the phase relations of the Fe–Cu–P alloy were evaluated using the Fe–Cu–P liquidus projection calculated with FactSage 8.2. Figure 7 shows the calculated Fe–Cu–P liquidus projection at 1 atm together with the compositions of the Fe–Cu–P alloy

before Cu removal and the Cu-depleted Fe–P alloy after refining. The initial alloy composition, containing approximately 7.57 wt.% P and 6.44 wt.% Cu, was located in the Fe-rich region of the ternary system. After Cu removal, the alloy composition shifted toward the Fe–P side, with the Cu content markedly reduced while P remained in the metallic phase. This compositional change confirmed that the sulfidation step selectively removed Cu but did not substantially remove P, thereby necessitating the subsequent oxidative dephosphorization step.

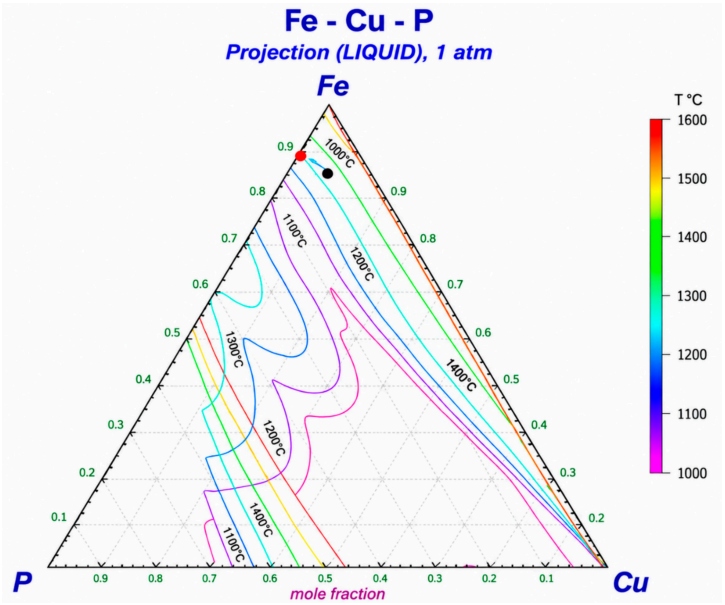


Figure 7. Calculated liquidus projection of the Fe–Cu–P system at 1 atm obtained using FactSage 8.2. The initial Fe–Cu–P alloy and the Cu-depleted Fe–P alloy after refining are indicated by the black and red filled circles, respectively.

The idealized sulfidation reaction was expressed as:

$$FeS(l) + 2Cu(l) \rightarrow Cu_2S(l) + Fe(l) \quad (14)$$

Because the actual sulfide product may consist of a Cu-rich matte or mixed Cu–Fe sulfide phase rather than stoichiometric Cu_2S, Reaction (14) was used as an idealized representation of Cu transfer. The thermodynamic preference for Cu sulfidation was evaluated by comparing the standard Gibbs energy changes for Cu_2S and FeS formation over the experimental temperature range. The formation reactions were expressed as follows:

$$2Cu(l) + \frac{1}{2}S_2(g) \rightarrow Cu_2S \quad (15)$$

$$Fe(l) + \frac{1}{2}S_2(g) \rightarrow FeS \quad (16)$$

As summarized in Table 5, the standard Gibbs energy change for Cu_2S formation was more negative than that for FeS formation throughout the temperature range of 1400–1600 °C. This result indicates that Cu has a greater thermodynamic affinity for sulfur than Fe under the investigated conditions. Therefore, the thermodynamic calculations suggest that sulfur supplied by FeS may preferentially react with Cu. However, because the sulfide-rich phase was not directly characterized, the detailed Cu partitioning and the specific sulfide phases formed cannot be conclusively confirmed in the present study.

Table 5. Standard Gibbs energy changes for Cu_2S and FeS formation calculated using HSC Chemistry 6.12.

Temperature (°C)	ΔG° for Cu_2S Formation (kJ mol^{-1})	ΔG° for FeS Formation (kJ mol^{-1})
1400	−82.480	−62.697
1500	−79.011	−59.196
1600	−75.546	−55.224

Based on the thermodynamic assessment, Cu-removal experiments were conducted at 1400, 1500, and 1600 °C. The Cu:FeS molar ratios were set at 2:1, 2:1.5, and 2:2 to evaluate the effects of stoichiometric and excess sulfur-source additions. An Fe_2SiO_4-based flux was added at approximately 6.01 g to promote the formation and separation of the sulfide-rich slag phase. For each experiment, 250 g of the Fe–Cu–P alloy was charged into an alumina crucible and melted at the target temperature. FeS was then added, and the sample was maintained for 3 h to promote the sulfidation reaction. Subsequently, the Fe_2SiO_4-based flux was added, and the sample was held at the same temperature for an additional 3 h. After cooling, the metallic and sulfide-rich phases were separated and characterized using SEM–EDS. The resulting Cu-depleted Fe–P alloy was used as the feed material for the subsequent oxidative dephosphorization experiments.

2.7. Oxidative Dephosphorization

2.7.1. Thermodynamic Basis for Phosphorus Oxidation

The Cu-depleted Fe–P alloy was subjected to oxidative dephosphorization using Fe_2O_3 as the oxidizing agent and a CaO–SiO_2-based slag. During the refining process, Fe_2O_3 supplied FeO to the slag, and phosphorus dissolved in the metallic phase was oxidized and transferred to the slag phase.

$$2[P]_{Fe} + 5FeO(l) \rightarrow P_2O_5 + 5Fe(l) \quad (17)$$

The standard Gibbs energy changes for Reaction (17), calculated using HSC Chemistry, are summarized in Table 6. The calculated ΔG° values increased with increasing temperature and remained positive over the investigated temperature range. At 1600 °C, the calculated value was 19.610 kcal mol^{-1}, corresponding to approximately 82.048 kJ mol^{-1}.

Table 6. Standard Gibbs energy changes for phosphorus oxidation by FeO calculated using HSC Chemistry.

Temperature (°C)	ΔG° for Reaction (17) (kJ mol^{-1})
1200	19.573
1300	35.020
1400	50.593
1500	66.270
1600	82.048

Note: The values were converted from kcal mol^{-1} to kJ mol^{-1} using 1 kcal = 4.184 kJ.

The positive Gibbs energy values indicate that phosphorus oxidation by FeO alone becomes thermodynamically less favorable as temperature increases under standard-state conditions. Therefore, Fe_2O_3 was selected as a stronger oxidizing agent to provide a sufficiently high oxygen potential for dephosphorization. Figure 8 compares the temperature dependence of the standard Gibbs energy changes associated with FeO, Fe_2O_3, and P_2O_5-related oxidation reactions calculated using FactSage 8.2. The substantially more negative

values associated with Fe_2O_3 formation indicate that Fe_2O_3 provides a higher oxidation potential than FeO over the investigated temperature range. This thermodynamic comparison supports the use of Fe_2O_3 as the oxidizing agent in the dephosphorization experiments.

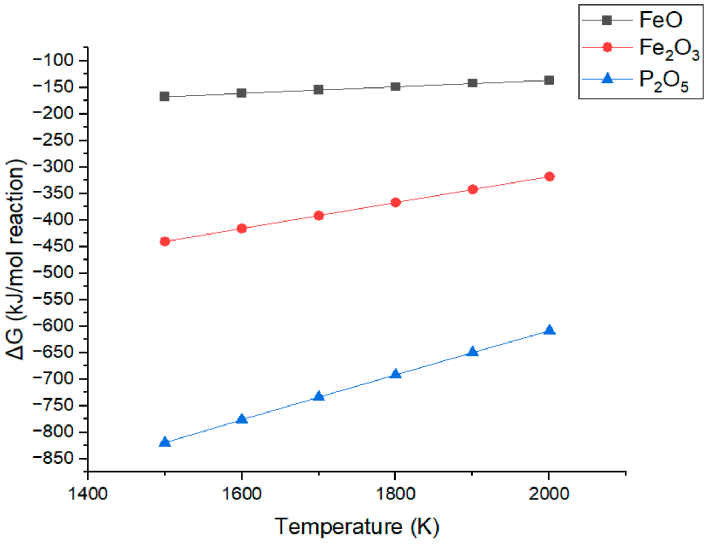


Figure 8. Temperature dependence of the standard Gibbs energy changes for the oxidation reactions considered in this study, calculated using FactSage 8.2 with the FToxid database.

2.7.2. Slag Design and Phosphorus Fixation

Following oxidation, P_2O_5 was stabilized in the CaO-containing slag. The idealized reaction for the formation of tricalcium phosphate was expressed as:

$$P_2O_5(l) + 3CaO(s) \rightarrow Ca_3(PO_4)_2(s) \quad (18)$$

Because the actual slag may contain several Ca–P–O phases depending on the temperature and slag composition, Reaction (18) was used as a simplified representation of phosphorus fixation in the basic slag. The phase relations of the CaO–SiO_2–P_2O_5 slag system were evaluated using FactSage 8.2. Figure 9 presents the calculated liquidus projection of the P_2O_5–CaO–SiO_2 system at 1 atm. The calculated diagram shows that the liquid-phase region and the stability of Ca–P–O-containing phases are strongly dependent on the CaO/SiO_2 ratio and P_2O_5 content. Based on this thermodynamic assessment, CaO–SiO_2 slags with basicities of 2.0, 2.5, and 3.0 were selected to evaluate the effects of basicity on phosphorus removal and Fe recovery.

2.7.3. Experimental Procedure for Dephosphorization

Premelted CaO–SiO_2-based slags were prepared at basicities,

$$B = \frac{CaO}{SiO_2}$$

with values of 2.0, 2.5, and 3.0. To minimize reactions between the CaO-containing slag and an alumina crucible, the dephosphorization experiments were conducted using an MgO crucible with a diameter of 5.0 cm and a height of 9.0 cm. The MgO crucible was placed inside an outer graphite crucible to form a double-crucible system and improve mechanical stability during high-temperature treatment. Unlike the conventional arrangement in which the metallic phase is placed beneath the slag, the premelted slag was placed at the bottom of the MgO crucible, and the Cu-depleted Fe–P alloy was positioned above the slag. This inverted arrangement was adopted to increase the effective contact area between

the molten metal and slag during the reaction. The crucible configuration is illustrated in Figure 10.

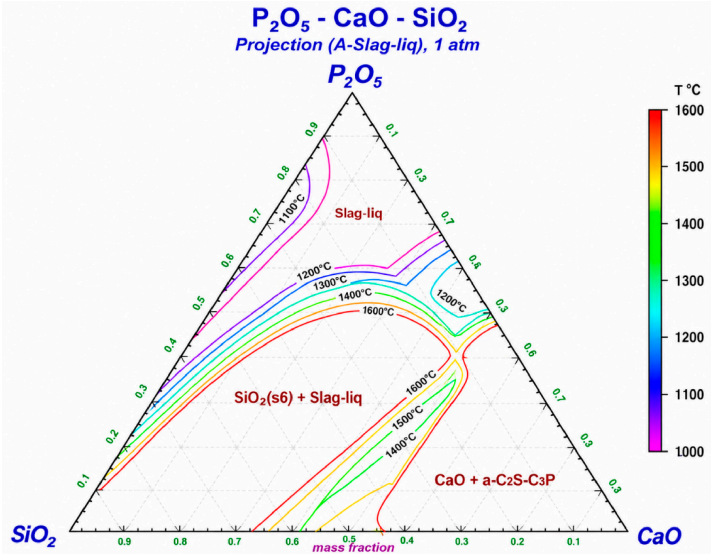


Figure 9. Calculated liquidus projection of the P_2O_5–CaO–SiO_2 system at 1 atm obtained using FactSage 8.2.

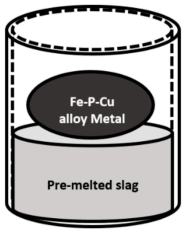


Figure 10. Schematic illustration of the arrangement of the Fe–P alloy and premelted slag inside the MgO crucible.

For each experiment, the premelted slag was prepared using 116.79 g of Fe_2O_3 as the oxidizing agent and 20.51 g of CaO. The amount of SiO_2 was adjusted according to the target basicity and was 10.26, 8.21, and 6.84 g for basicities of 2.0, 2.5, and 3.0, respectively. The premelted slag was first charged into the bottom of the MgO crucible, after which the Cu-depleted Fe–P alloy was placed above the slag. The crucible assembly was positioned at the center of the uniform-temperature zone of the vertical tube furnace. Before heating, the reaction tube was thoroughly purged with Ar to remove residual air. The sample was then heated to the target temperature under a continuous Ar atmosphere, while the reaction temperature was continuously monitored and controlled using a Type C thermocouple. During dephosphorization, phosphorus in the metallic phase was oxidized by Fe_2O_3-derived oxidizing species and transferred to the slag as P_2O_5-containing species. The oxidized phosphorus was subsequently stabilized by CaO-containing slag components as Ca-P-O compounds. The sample was maintained at the target temperature for 3 h to allow sufficient reaction and phase separation between the metallic and slag phases. After completion of the reaction, the sample was furnace-cooled under an Ar atmosphere. Because the metallic and slag phases were mutually immiscible and formed macroscopically distinct solidified phases after cooling, they were manually separated after removal from the crucible without the use of special separation equipment and were subsequently weighed. The recovered metallic phase was designated as the refined Fe product and was subjected to subsequent chemical-composition and microstructural analyses. The same procedure was repeated for each slag-basicity condition to evaluate the effects of basicity on phosphorus

removal and Fe recovery. The chemical composition of the recovered metallic phase was quantitatively analyzed using inductively coupled plasma–optical emission spectrometry (ICP–OES; Optima 8300, PerkinElmer, Waltham, MA, USA). The measured compositions and recovered phase masses were used to calculate the phosphorus removal efficiency, Fe loss, and Fe recovery.

3. Results and Discussion

3.1. Production and Preliminary Refining of the Fe-Based Alloy

The spent LFP battery-derived material was subjected to oxidative smelting to separate a Cu-rich phase from an FeO-rich slag. After treatment, 29.49 g of the Cu-rich phase and 32.79 g of the slag phase were recovered, indicating clear macroscopic phase separation. The chemical compositions of the recovered products determined by XRF are summarized in Table 7. The Cu-rich phase contained 67.8 wt.% Cu and 20.5 wt.% Fe, whereas the slag phase contained 53.9 wt.% Fe, 18.75 wt.% P, and 17.72 wt.% Si. These results indicate that Cu was preferentially concentrated in the dense metallic or speiss-like phase, while a large proportion of Fe was retained in the oxide-rich slag. Phosphorus was distributed between the two products, with 7.03 wt.% P detected in the Cu-rich phase and 18.75 wt.% P in the slag. The observed distribution demonstrates that oxidative smelting was effective for the primary separation of Cu from Fe. However, the presence of P in both products indicates that oxidative phase separation alone was insufficient to achieve complete phosphorus removal.

Table 7. Chemical compositions of the Cu-rich and slag phases obtained after oxidative smelting, determined by XRF.

Cu-Rich Phase		Slag Phase	
Element	**Content (wt.%)**	**Element**	**Content (wt.%)**
Cu	67.8	Fe	53.9
Fe	20.5	P	18.75
P	7.03	Si	17.72
Ni	1.78	Cu	5.92
S	1.25	S	1.98
Co	0.98	Co	1.02
Cr	0.66	Cr	0.71

The FeO-rich slag was subsequently subjected to carbothermic reduction in the presence of carbon and CaO. Representative SEM images and local EDS elemental distributions of the resulting metallic and slag phases are presented in Figure 11, and the corresponding SEM–EDS area-analysis results are summarized in Table 8. Because the available observations were obtained from the original SEM–EDS images rather than from mounted and polished cross-sections, the microstructural features and phase distributions are interpreted qualitatively. The analyzed metallic region contained 81.36 wt.% Fe, indicating substantial Fe enrichment in the metallic phase after carbothermic reduction. However, the metallic phase also contained 12.14 wt.% P and 6.04 wt.% Cu. These local compositional results suggest that P- and Cu-containing species were also present in the reduced metallic phase. In contrast, the analyzed slag region was predominantly composed of O, Ca, and Si, with 6.39 wt.% P and only 0.83 wt.% Fe. The local enrichment of Ca, Si, O, and P is consistent with the presence of Ca–Si–P–O-containing slag constituents; however, specific phase identities cannot be conclusively assigned from the present SEM–EDS data alone. The results suggest that CaO addition contributed to partial retention of P in the slag; however, P was also detected at a relatively high concentration in the metallic phase after reduction.

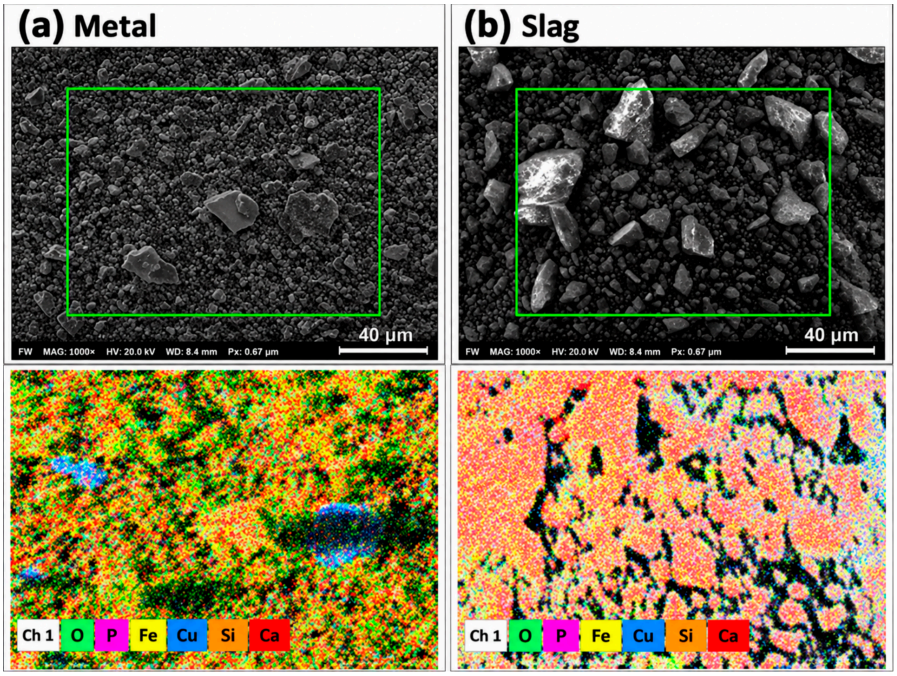


Figure 11. Representative SEM images and EDS elemental maps of the (**a**) metallic and (**b**) slag phases obtained af-ter carbothermic reduction of the FeO-rich slag. The green boxes indicate the regions selected for EDS elemental mapping. The images provide qualitative local compositional information.

Table 8. Chemical compositions of the metallic and slag phases obtained after carbothermic reduction, determined by SEM–EDS area analysis.

Metallic Phase		Slag Phase	
Element	**Content (wt.%)**	**Element**	**Content (wt.%)**
Fe	81.36	O	44.53
P	12.14	Ca	37.12
Cu	6.04	Si	11.08
Ca	0.24	P	6.39
Si	0.22	Fe	0.83
-	-	Cu	0.05

Because the metallic phase obtained by carbothermic reduction still contained a high P concentration, a preliminary oxygen-blowing treatment was conducted. Representative SEM images and local EDS elemental distributions of the metallic and slag phases after oxygen blowing are shown in Figure 12, and the corresponding SEM–EDS area compositions are summarized in Table 9. Because the available characterization was performed on surface/particle regions rather than on mounted and polished cross-sections, the microstructural features and phase distributions are interpreted qualitatively. After oxygen blowing, the P content in the analyzed metallic region decreased from 12.14 to 7.96 wt.%, while the Fe content increased from 81.36 to 85.38 wt.%. The analyzed slag region contained 11.20 wt.% P, compared with 6.39 wt.% P in the slag analyzed before oxygen blowing. These local compositional changes are consistent with partial oxidation of P in the metallic phase and its enrichment in the slag during oxygen blowing; however, the detailed phase distribution and individual slag-phase identities cannot be conclusively determined from the present surface SEM–EDS observations alone.

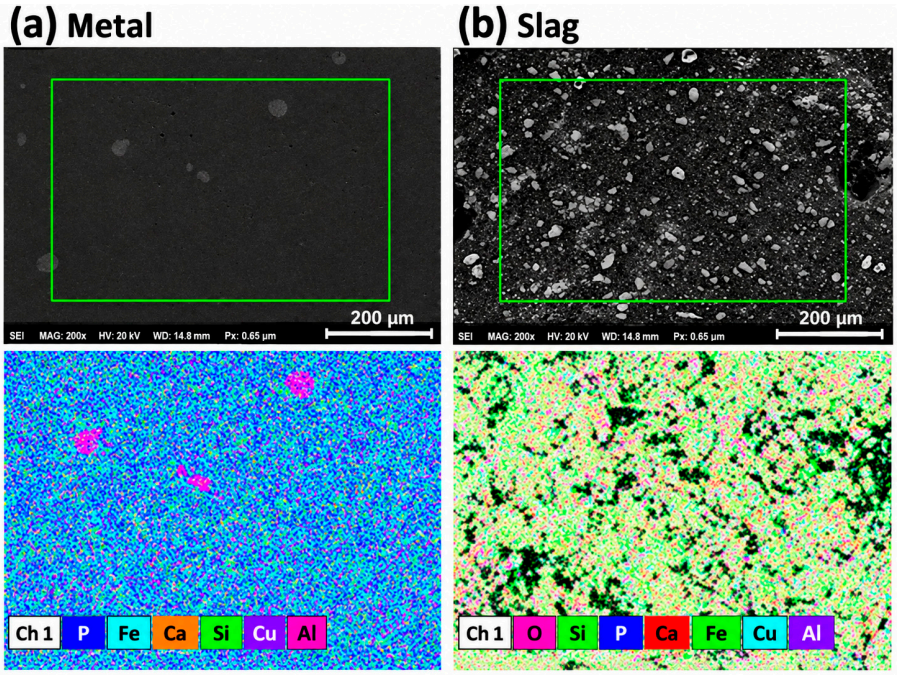


Figure 12. Representative SEM images and EDS elemental maps of the (**a**) metallic and (**b**) slag phases obtained after preliminary oxygen blowing. The images provide qualitative local compositional information.

Table 9. Chemical compositions of the metallic and slag phases obtained after preliminary oxygen blowing, determined by SEM–EDS area analysis.

Metallic Phase		Slag Phase	
Element	**Content (wt.%)**	**Element**	**Content (wt.%)**
Fe	85.38	O	37.27
P	7.96	Ca	36.6
Cu	6.55	Si	11.72
Al	0.05	P	11.2
Ca	0.04	Al	2.19
Si	0.03	Fe	0.96
-	-	Cu	0.06

The apparent P reduction based on the SEM–EDS area compositions can be estimated as:

$$R_{P,preliminary} = \frac{12.14 - 7.96}{12.14} \times 100 = 34.4\% \quad (19)$$

Thus, the preliminary oxygen-blowing treatment reduced the local P concentration in the metallic phase by approximately 34.4%. Nevertheless, the residual P content of 7.96 wt.% remained too high for direct utilization of the Fe-rich product. This result confirms that oxygen blowing alone was insufficient and that a subsequent controlled oxidative dephosphorization step using Fe_2O_3 and a $CaO–SiO_2$-based slag was required. The combined results demonstrate that the pyrometallurgical treatment successfully converted Fe present in the spent LFP battery material into an Fe-rich metallic phase. Oxidative smelting preferentially separated Cu into a Cu-rich phase, while carbothermic reduction recovered Fe from the FeO-rich slag. However, P and residual Cu were simultaneously transferred to the metallic phase. Preliminary oxygen blowing partially decreased the P concentration but did not achieve sufficient purification. Therefore, sequential Cu removal and controlled oxidative dephosphorization were required to obtain a purified Fe product.

3.2. Selective Cu Removal from the Fe–Cu–P Alloy

The Fe–Cu–P alloy obtained after the preceding pyrometallurgical treatment still contained a considerable amount of Cu, which could limit the subsequent purification and utilization of the Fe-rich product. Therefore, selective Cu removal was investigated through FeS-assisted sulfidation followed by slag refining. The effects of reaction temperature and FeS addition on the composition and microstructural characteristics of the refined metallic phase were systematically evaluated. The Cu-removal experiments were conducted at 1400, 1500, and 1600 °C using Cu molar ratios of 2:1, 2:1.5, and 2:2. SEM images and EDS elemental maps of the recovered metallic phases are compared in Figure 13, while the corresponding SEM–EDS area compositions are summarized in Table 10. These Cu-removal results were previously reported in our earlier study [15] and are included here to provide continuity within the integrated refining sequence and to support discussion of the subsequent dephosphorization step. To facilitate direct comparison of the effects of temperature and FeS addition, the SEM–EDS results obtained under the nine experimental conditions were combined into a single composite figure.

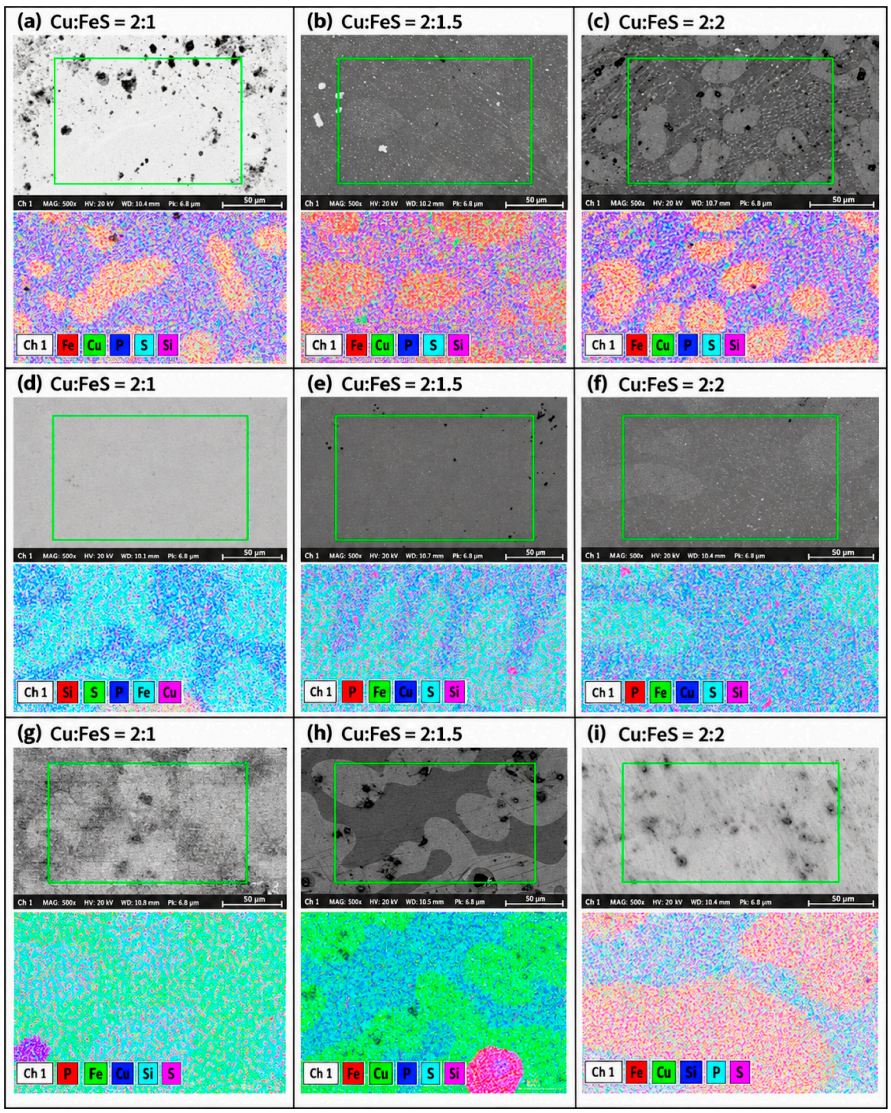


Figure 13. SEM images and EDS elemental maps of the metallic phases obtained after FeS-assisted Cu removal at different temperatures and Cu molar ratios: (**a**–**c**) 1400 °C, (**d**–**f**) 1500 °C, and (**g**–**i**) 1600 °C. Within each tempera-ture range, the Cu molar ratios were 2:1, 2:1.5, and 2:2, respectively. This figure combines results from the present study with previously published data adapted from Ref. [15].

Table 10. Local SEM–EDS area compositions of the metallic phases obtained under different Cu-removal conditions. Adapted from Ref. [15].

Temperature (°C)	Cu Molar Ratio	Fe (wt.%)	P (wt.%)	Cu (wt.%)	S (wt.%)	Si (wt.%)
1400	2:1.0	90.80	7.55	1.47	0.15	0.03
1400	2:1.5	89.40	7.36	2.77	0.4	0.07
1400	2:2.0	88.98	7.29	2.97	0.72	0.04
1500	2:1.0	89.15	7.51	3.21	0.22	0.11
1500	2:1.5	88.77	7.12	3.62	0.43	0.07
1500	2:2.0	88.19	7.08	3.78	0.85	0.1
1600	2:1.0	88.43	7.02	4.27	0.21	0.07
1600	2:1.5	87.83	7.13	4.55	0.4	0.09
1600	2:2.0	87.28	6.84	5.04	0.84	0.1

Note: The reported values represent local area compositions determined by SEM–EDS and should not be interpreted as bulk compositions of the entire metallic products.

Because the compositions summarized in Table 10 were obtained by SEM–EDS area analysis, they represent local compositions of the analyzed regions rather than bulk compositions of the entire recovered metallic products. Accordingly, these data were used only to compare the relative effects of reaction temperature and FeS addition on the local composition of the metallic phase. They should not be used alone for quantitative evaluation of the overall Cu-removal efficiency or Cu mass balance. A rigorous determination of the overall Cu distribution and removal efficiency would require bulk chemical analysis of representative metallic and sulfide-rich products.

Among the investigated conditions, the metallic phase obtained at 1400 °C with a Cu:FeS molar ratio of 2:1 exhibited the lowest local Cu concentration by SEM–EDS area analysis. Under this condition, the analyzed metallic region contained 90.80 wt.% Fe, 7.55 wt.% P, 1.47 wt.% Cu, 0.15 wt.% S, and 0.03 wt.% Si. This condition also showed the highest local Fe concentration and a relatively low local S concentration among the investigated conditions.

At 1400 °C, increasing the FeS addition beyond the Cu molar ratio of 2:1 did not further decrease the local Cu concentration. The Cu concentration increased from 1.47 wt.% at a ratio of 2:1 to 2.77 and 2.97 wt.% at ratios of 2:1.5 and 2:2, respectively. At the same time, the local S concentration increased from 0.15 to 0.40 and 0.72 wt.%, respectively. These results indicate that, within the analyzed regions, excessive FeS addition did not produce a further decrease in Cu and was accompanied by increased S retention in the metallic phase. A similar tendency was observed at 1500 and 1600 °C. At 1500 °C, the local Cu concentration increased from 3.21 wt.% at a Cu ratio of 2:1 to 3.78 wt.% at a ratio of 2:2, while the S concentration increased from 0.22 to 0.85 wt.%. At 1600 °C, the local Cu concentration increased from 4.27 to 5.04 wt.% as the Cu ratio changed from 2:1 to 2:2. The local S content also increased from 0.21 to 0.84 wt.%. These results suggest that increasing the amount of FeS beyond the 2:1 condition did not improve the relative Cu-removal behavior under the present experimental conditions. Excess FeS may increase sulfur dissolution or retention in the metallic phase and may also influence the physical separation of the sulfide-rich phase from the Fe-rich metallic phase. However, because the SEM–EDS results represent local compositions of the metallic phase, the exact bulk distribution of Cu and S between the metallic and sulfide-rich phases cannot be conclusively determined from these data alone. The effect of reaction temperature was also significant. At a fixed Cu molar ratio of 2:1, the local Cu concentration increased from 1.47 wt.% at 1400 °C to 3.21 wt.% at 1500 °C and 4.27 wt.% at 1600 °C. Concurrently, the Fe concentration decreased from 90.80 wt.% at 1400 °C to 89.15 wt.% at 1500 °C and 88.43 wt.% at 1600 °C. Similar temperature-dependent behavior was observed for the other FeS addition levels. The deterioration in the observed Cu-removal trend at higher temperatures may be associated with changes in the equilibrium

distribution of Cu between the metallic and sulfide-rich phases, as well as increased mutual solubility between these phases. In addition, the effectiveness of phase separation during cooling may affect the amount of residual Cu detected in the recovered metallic product. Thus, within the investigated temperature range, 1400 °C provided the most favorable relative Cu-removal behavior based on the local SEM–EDS results.

This trend is consistent with our previous sulfidation–slag refining study on an Fe–P–Cu alloy recovered from spent LFP batteries [15]. In that study, the most favorable condition was likewise obtained at 1400 °C and a Cu:FeS molar ratio of 2:1, where the recovered metallic phase contained 90.80 wt.% Fe and 1.47 wt.% Cu. In that previous work, bulk mass-balance evaluation was used to quantify an Fe recovery of 87.42% and a Cu-removal efficiency of 81.13% [15]. The agreement in the optimum temperature and FeS dosage between the two studies supports the conclusion that excessive FeS addition and higher treatment temperatures are unfavorable for selective Cu removal under the investigated conditions. Importantly, the present study extends the previous Cu-removal investigation by incorporating the Cu-removal step into a broader sequential refining route that includes subsequent oxidative dephosphorization. Therefore, the Cu-removal results in the present work are used primarily to establish the appropriate pretreatment condition for the following P-removal stage rather than to provide an independent bulk Cu mass balance. Although the observed compositional trends are consistent with selective Cu sulfidation, direct characterization of the sulfide-rich phase would be required to confirm Cu partitioning and identify the sulfide phases formed during refining. Overall, among the investigated conditions, 1400 °C and a Cu:FeS molar ratio of 2:1 produced the lowest local Cu concentration observed by SEM–EDS area analysis. Under this condition, the analyzed metallic phase also exhibited the highest local Fe concentration and a relatively low S concentration. These findings are consistent with the previously reported sulfidation–slag refining behavior [15] and provide the basis for selecting the Cu-depleted Fe–P alloy for the subsequent oxidative dephosphorization step.

Cu-Removal Efficiency Under the Optimum Condition

The Cu-removal efficiency under the optimum condition was estimated by considering both the mass of the recovered metallic phase and its Cu concentration before and after sulfidation. The Cu-removal efficiency was defined as:

$$Cu\ removal\ efficiency(\%) = \left[\frac{initial\ Cu\ mass - final\ Cu\ mass}{initial\ Cu\ mass}\right] \times 100 \quad (20)$$

where the initial Cu mass and final Cu mass represent the Cu masses in the metallic phase before and after Cu removal, respectively.

The initial Fe–Cu–P alloy weighed 250 g and contained 6.44 wt.% Cu. Therefore, the initial Cu mass was calculated as:

$$Initial\ Cu\ mass = 250\ \text{g} \times (6.44/100) = 16.10\ \text{g} \quad (21)$$

After treatment at 1400 °C using a Cu molar ratio of 2:1, the recovered metallic phase weighed 246.992 g and contained 1.47 wt.% Cu. Therefore, the residual Cu mass was calculated as:

$$Final\ Cu\ mass = 246.992\ \text{g} \times (1.47/100) = 3.63\ \text{g} \quad (22)$$

Accordingly, the Cu-removal efficiency was:

$$Cu\ removal\ efficiency = [(16.10 - 3.63)/16.10] \times 100 = 77.45\% \quad (23)$$

The FeS-assisted sulfidation process therefore substantially decreased the Cu content of the Fe–Cu–P alloy. Under the optimum condition, the metallic phase contained 90.80 wt.% Fe and 1.47 wt.% Cu, while the residual S content was limited to 0.15 wt.%. The slight differences in elemental concentrations determined by SEM–EDS should be interpreted with caution because SEM–EDS represents local area compositions rather than bulk chemical compositions. Therefore, the calculated Cu-removal efficiency should be regarded as an estimate based on the measured metallic-phase mass and SEM–EDS Cu concentration. Bulk chemical analysis of the optimum metallic product by ICP–OES or XRF would provide a more rigorous evaluation of the overall Cu mass balance. Nevertheless, the Cu-removal results clearly demonstrate the effectiveness of FeS-assisted sulfidation for reducing Cu contamination in the Fe-rich alloy. The refined alloy still contained 7.55 wt.% P, indicating that selective Cu removal alone was insufficient to produce a purified Fe product. Consequently, the Cu-depleted Fe–P alloy obtained under the optimum condition was subsequently subjected to controlled oxidative dephosphorization using Fe_2O_3 and a CaO–SiO_2-based slag.

3.3. Effect of Slag Basicity on Dephosphorization

Following selective Cu removal, the resulting Cu-depleted Fe–P alloy still contained approximately 7.55 wt.% P. Therefore, oxidative dephosphorization was conducted using Fe_2O_3 as the oxidizing agent and a CaO–SiO_2-based slag. The effect of slag basicity, defined as the mass ratio of CaO to SiO_2, was investigated at basicity values of 2.0, 2.5, and 3.0. The compositions of the refined metallic phases obtained at different slag basicities are summarized in Table 11. A pronounced decrease in the residual P content was observed with increasing slag basicity. At B = 2.0, the P content of the metallic phase was 1.33 wt.%. Increasing the basicity to 2.5 reduced the P content to 0.20 wt.%, while a further increase to B = 3.0 decreased the residual P concentration to only 0.042 wt.%. These results demonstrate that increasing the CaO/SiO_2 ratio strongly enhanced the dephosphorization of the Cu-depleted Fe–P alloy.

Table 11. Effect of slag basicity on the composition of the metallic phase after dephosphorization.

Basicity, B = CaO/SiO_2	P (wt.%)	Cu (wt.%)	S (wt.%)	Si (wt.%)
2	1.330	1.69	0.008	0.011
2.5	0.200	2.13	0.005	0.008
3	0.042	1.40	0.004	0.006

The strong decrease in the residual P concentration with increasing basicity can be attributed to the greater capacity of the CaO-rich slag to stabilize oxidized phosphorus species. During oxidative refining, phosphorus in the metallic phase is oxidized by Fe_2O_3-derived oxygen-bearing species and transferred to the slag. The oxidized phosphorus can subsequently react with basic CaO-containing species to form stable Ca–P–O compounds, thereby decreasing the activity of phosphorus oxides in the slag and promoting further phosphorus transfer from the metallic phase. It is important to note that the amount of CaO was maintained constant in the present experiments, whereas the amount of SiO_2 was varied to adjust the slag basicity. Therefore, the increase in basicity represents an increase in the relative CaO/SiO_2 ratio rather than an increase in the absolute amount of CaO. The resulting change in slag composition enhanced the ability of the slag to retain oxidized phosphorus.

The observed enhancement of dephosphorization with increasing slag basicity is consistent with previous studies on hot-metal refining using CaO–SiO_2–FeO_x-based slags. Zhang et al. [16] reported that effective phosphorus removal depends on the combined effects of oxidation potential and slag chemistry and demonstrated that Fe_2O_3 addition

can promote dephosphorization even under relatively low-basicity conditions. Similarly, Wang et al. [17] showed that phosphorus distribution in CaO–SiO_2–FeO_x-based slags is strongly governed by slag composition, particularly the basic oxide/SiO_2 balance and the availability of oxidizing species. In the present study, increasing the CaO/SiO_2 ratio from 2.0 to 3.0 decreased the residual P content from 1.33 to 0.042 wt.% and increased the P removal efficiency from 86.55% to 99.44%. These results are therefore consistent with established dephosphorization principles and demonstrate that sufficiently high basicity, together with Fe_2O_3-derived oxidation potential, can also be effectively applied to an Fe-rich alloy recovered from spent LFP batteries. The residual S and Si contents also decreased slightly with increasing basicity. The S content decreased from 0.008 wt.% at B = 2.0 to 0.004 wt.% at B = 3.0, while the Si content decreased from 0.011 to 0.006 wt.%. In contrast, the residual Cu content showed no monotonic dependence on slag basicity, varying from 1.69 wt.% at B = 2.0 to 2.13 wt.% at B = 2.5 and 1.40 wt.% at B = 3.0. Thus, the principal effect of increasing slag basicity was associated with phosphorus removal rather than Cu removal. This behavior also confirms the intended functional separation of the sequential refining stages: most of the Cu removal was achieved during the preceding FeS-assisted sulfidation step, whereas the subsequent basic oxidative refining stage primarily controlled phosphorus removal. The results therefore demonstrate that selective sulfidation and oxidative dephosphorization serve complementary roles within the integrated refining route.

3.3.1. Phosphorus Distribution Between the Metal and Slag Phases

To quantitatively evaluate phosphorus partitioning between the metallic and slag phases, the phosphorus distribution ratio, (L_P), was calculated as:

$$L_P = (\text{wt.\% } P \text{ in slag})/(\text{wt.\% } P \text{ in metal}) \quad (24)$$

The calculated phosphorus distribution ratios are summarized in Table 12.

Table 12. Phosphorus distribution ratio calculated from bulk chemical analyses of the metallic and slag phases as a function of slag basicity.

Basicity, B = CaO/SiO_2	P in Metal (wt.%)	P in Slag (wt.%)	Lp
2	1.330	4.470	3.36
2.5	0.200	5.200	26.00
3	0.042	5.820	138.57

The phosphorus distribution ratio increased sharply with increasing slag basicity. (Lp) increased from 3.36 at (B = 2.0) to 26.00 at (B = 2.5), and reached 138.57 at (B = 3.0). This pronounced increase indicates that phosphorus was increasingly partitioned into the slag phase as the CaO/SiO_2 ratio increased. The increase in (Lp) is consistent with the enhanced stabilization of oxidized phosphorus in the CaO-containing slag. At higher basicity, the chemical activity of phosphorus oxide in the slag is reduced through the formation of stable Ca–P–O species, thereby shifting the metal–slag phosphorus partitioning toward the slag phase. In particular, the very high (L_P) value obtained at (B = 3.0) is consistent with the very low residual P concentration of 0.042 wt.% in the metallic phase. These results indicate that effective dephosphorization is governed not only by the oxidation of phosphorus in the metallic phase but also by the ability of the slag to chemically retain the oxidized phosphorus species.

3.3.2. Phosphorus Removal Efficiency

The overall phosphorus removal efficiency was evaluated by comparing the phosphorus mass in the Cu-depleted Fe–P alloy before dephosphorization with that remaining in the refined metallic phase after treatment. The phosphorus removal efficiency was defined as:

$$P\ removal\ efficiency(\%) = \left[\frac{initial\ P\ mass - final\ P\ mass}{initial\ P\ mass}\right] \times 100 \quad (25)$$

The calculated phosphorus removal efficiencies are summarized in Table 13.

Table 13. Phosphorus removal efficiency as a function of slag basicity.

Basicity, B = CaO/SiO_2	Initial P Mass in Fe–P Alloy (g)	Residual P Mass in Refined Metal (g)	P Removal Efficiency (%)
2	7.55	1.02	86.55
2.5	7.55	0.12	98.43
3	7.55	0.04	99.44

Note: The P removal efficiencies were calculated using the unrounded analytical values; therefore, slight differences may arise when the rounded values shown in the table are used for recalculation.

The phosphorus removal efficiency increased substantially with increasing slag basicity. At (B = 2.0), 86.55% of the initial phosphorus was removed from the metallic phase. Increasing the basicity to 2.5 increased the removal efficiency to 98.43%, while the highest basicity of (B = 3.0) resulted in a phosphorus removal efficiency of 99.44%. The consistent trends observed in the residual P concentration, phosphorus distribution ratio, and phosphorus removal efficiency demonstrate that slag basicity plays a dominant role in controlling the dephosphorization behavior of the Cu-depleted Fe–P alloy. At higher basicity, phosphorus was more effectively oxidized and stabilized in the slag phase, resulting in a strong shift of phosphorus from the metallic phase to the slag. Among the investigated conditions, (B = 3.0) provided the most effective dephosphorization performance, reducing the residual P concentration to 0.042 wt.% and achieving a phosphorus removal efficiency of 99.44%. These results confirm that controlling the CaO/SiO_2 ratio is critical for achieving deep dephosphorization and further purification of the Fe-rich metallic product.

3.4. Calculated Fe Content and Recovery Evaluation

To evaluate the overall effectiveness of the sequential pyrometallurgical refining process, the chemical composition and Fe recovery of the metallic products were evaluated after the final oxidative dephosphorization step. The residual concentrations of P, Cu, S, and Si in the refined metallic products were determined by bulk ICP–OES analysis. The Fe content was subsequently calculated by difference from the measured concentrations of these major residual impurities rather than being determined directly by complete elemental analysis. Accordingly, the calculated Fe content and estimated Fe recovery were evaluated as a function of slag basicity. The overall compositions and Fe recovery results are summarized in Table 14. As the slag basicity increased from 2.0 to 3.0, the calculated Fe content of the recovered metallic product increased from 96.96 to 98.55 wt.%. This improvement was primarily associated with the substantial decrease in the residual P content, which decreased from 1.33 wt.% at a basicity of 2.0 to only 0.042 wt.% at a basicity of 3.0. The concentrations of S and Si were also maintained at very low levels under all conditions.

Table 14. Effect of slag basicity on the bulk composition, calculated Fe content, and estimated Fe recovery of the refined metallic product.

Basicity (CaO/SiO_2)	P (wt.%)	Cu (wt.%)	S (wt.%)	Si (wt.%)	Calculated Fe Content (wt.%)	Estimated Recovered Fe Mass (g)	Estimated Fe Recovery (%)
2	1.33	1.69	0.008	0.011	96.96	18.85	91.77
2.5	0.20	2.13	0.005	0.008	97.66	18.99	92.43
3	0.042	1.40	0.004	0.006	98.55	19.16	93.27

Note: P, Cu, S, and Si concentrations were determined by bulk ICP–OES. The Fe content was calculated by difference from the measured major residual impurities and was not determined by direct total-Fe analysis. The recovered Fe mass and Fe recovery were therefore estimated using the calculated Fe contents and unrounded experimental values. The initial Fe mass in the spent LFP battery feed was 20.55 g.

The Fe content was calculated by difference from the measured concentrations of the major residual impurities, P, Cu, S, and Si. Because a complete elemental inventory and direct determination of total Fe were not performed, the calculated values should not be interpreted as rigorously determined bulk Fe purity. Accordingly, the increase in calculated Fe content with increasing slag basicity was dominated by the progressive removal of P. In particular, the decrease in P from 1.33 wt.% at a basicity of 2.0 to 0.042 wt.% at a basicity of 3.0 contributed substantially to the increase in calculated Fe content from 96.96 to 98.55 wt.%. The Cu content did not exhibit a monotonic dependence on slag basicity, varying from 1.69 wt.% at a basicity of 2.0 to 2.13 wt.% at 2.5 and decreasing to 1.40 wt.% at 3.0. This behavior indicates that the final dephosphorization stage primarily controlled phosphorus removal, whereas a substantial decrease in Cu had been observed during the preceding FeS-assisted sulfidation step. Therefore, the improvement in calculated Fe content during dephosphorization should be attributed mainly to P removal rather than to further Cu removal.

The Fe recovery was calculated according to:

$$Fe\ recovery(\%) = (\frac{mass\ of\ Fe\ in\ the\ recoverd\ metallic\ product}{initial\ Fe\ mass\ in\ the\ spent\ LFP\ feed}) \times 100 \quad (26)$$

The initial Fe mass in the spent LFP battery feed was 20.55 g. Based on the calculated Fe contents of the recovered metallic products, the recovered Fe masses were estimated to be 18.85, 18.99, and 19.16 g at basicities of 2.0, 2.5, and 3.0, respectively. The corresponding estimated Fe recoveries were 91.77%, 92.43%, and 93.27%, respectively. Because the recovered Fe masses were derived using the calculated Fe contents rather than directly measured total Fe concentrations, these recovery values should also be regarded as estimates based on the available bulk impurity analyses.

The estimated Fe recovery remained above 91% under all investigated conditions and showed a slight increase with increasing slag basicity. Within the limitations of the present analytical approach, this trend suggests that the enhancement of phosphorus removal at higher basicity was not accompanied by a substantial loss of Fe from the recovered metallic product. In particular, the basicity of 3.0 achieved both the highest calculated Fe content and the highest estimated Fe recovery among the investigated conditions. The simultaneous increase in calculated Fe content and estimated Fe recovery with increasing basicity suggests that control of slag chemistry was important not only for phosphorus removal but also for maintaining Fe in the recovered metallic phase. A higher CaO/SiO_2 ratio enhanced the stabilization of oxidized phosphorus in the slag, thereby promoting deep dephosphorization while maintaining a high recovery of the metallic product.

The relatively high retention of Fe is consistent with the intended role of $CaO–SiO_2–FeO_x$-based dephosphorization slags, in which phosphorus removal must be promoted

without excessive oxidation of Fe. Previous studies of hot-metal dephosphorization have likewise emphasized the combined importance of oxidation potential and slag basicity in increasing phosphorus transfer to the slag while limiting undesirable Fe oxidation [16,17]. Although the present Fe recovery values cannot be compared directly with those studies because the feed composition, slag system, process boundary, and analytical basis differ, the present trend is consistent with the general metallurgical requirement that deep dephosphorization be achieved while retaining most of the Fe in the metallic phase. A comparison with the preceding Cu-removal stage also illustrates the complementary functions of the two refining steps. In our previous FeS-assisted sulfidation–slag refining study [15], an Fe recovery of 87.42% was obtained under the optimum Cu-removal condition of 1400 °C and a Cu:FeS molar ratio of 2:1. The estimated Fe recovery of 93.27% obtained after the present dephosphorization stage should not be interpreted as directly superior because the two values correspond to different process boundaries and analytical bases. Nevertheless, both results indicate that selective impurity removal can be achieved while retaining a large fraction of Fe in the metallic product.

Despite the use of Fe_2O_3 as an oxidizing agent, the estimated Fe recovery remained relatively high, suggesting that extensive loss of Fe from the recovered metallic phase was limited under the selected refining conditions. However, the present results do not directly establish the detailed oxidation kinetics of Fe and P; rather, they demonstrate experimentally that an appropriate combination of oxidation potential and slag basicity enabled efficient P removal while retaining a large fraction of the Fe in the metallic product. From the perspective of the overall process, the sequential refining strategy reduced the two major impurities, Cu and P, in the Fe-rich alloy derived from spent LFP batteries. Cu was first reduced through FeS-assisted sulfidation, after which P was removed through oxidative slag refining. Under the optimum dephosphorization condition at a slag basicity of 3.0, the final metallic product contained 0.042 wt.% P, 1.40 wt.% Cu, 0.004 wt.% S, and 0.006 wt.% Si, corresponding to a calculated Fe content of 98.55 wt.% based on the measured major residual impurities and an estimated Fe recovery of 93.27%.

Although the residual Cu concentration of 1.40 wt.% represents a substantial decrease relative to the Cu-containing precursor alloy, it remains higher than the level typically preferred for direct use in many conventional steel grades. Residual Cu is generally undesirable in steelmaking because excessive Cu can promote surface hot-shortness during high-temperature processing [13]. Therefore, the recovered metallic product should be regarded more appropriately as a recyclable Fe-bearing secondary resource or blended scrap feed rather than as a direct substitute for low-Cu steelmaking feed. By blending the recovered product with low-Cu scrap or virgin Fe sources at an appropriate ratio, the overall Cu concentration of the steelmaking charge could be reduced to a level suitable for the intended steel grade. These results demonstrate that the combination of FeS-assisted Cu removal and controlled oxidative dephosphorization provides an effective route for upgrading Fe recovered from spent LFP batteries. In particular, the results highlight the importance of slag-basicity control for simultaneously achieving deep phosphorus removal, a high calculated Fe content, and limited estimated Fe loss during the final refining stage. Compared with most spent-LFP recycling approaches, which primarily emphasize Li recovery, cathode-material regeneration, or separation of Li, Fe, and P [4–12], the present work focuses specifically on the downstream metallurgical upgrading of the recovered Fe-bearing fraction. The integrated sequence of selective Cu sulfidation followed by oxidative dephosphorization therefore represents a different utilization strategy in which recovered Fe is converted into a recyclable metallic secondary resource.

Overall, the sequential refining process exploited the different chemical affinities of Cu and P to achieve selective impurity removal. The observed decrease in Cu concentration in

the metallic phase was consistent with preferential Cu sulfidation during the FeS-assisted treatment, whereas P was subsequently oxidized and stabilized in the CaO-rich slag during oxidative dephosphorization. Because the sulfide-rich phase was not directly characterized by SEM–EDS or XRD, the detailed Cu distribution and the identity of the sulfide phases remain to be confirmed. The agreement between the thermodynamic predictions, the experimental trends, and established metallurgical principles reported in previous studies [13,15–17] supports the feasibility of sequential sulfidation followed by basic slag refining for upgrading Fe recovered from spent LFP batteries. Further work should include direct total-Fe analysis, bulk Cu mass-balance validation, direct characterization of the sulfide-rich phase, optimization of residual Cu removal, and evaluation of blending strategies for practical steelmaking applications.

4. Conclusions

An integrated pyrometallurgical refining process was investigated for the recovery and upgrading of an Fe-rich metallic product from spent $LiFePO_4$ (LFP) battery materials. The process combined the production of an Fe-rich alloy, selective Cu removal through FeS-assisted sulfidation, and subsequent oxidative dephosphorization using Fe_2O_3 and a $CaO–SiO_2$-based slag. The principal conclusions are summarized as follows.

FeS-assisted sulfidation decreased the Cu concentration observed in the metallic phase. Among the investigated conditions, 1400 °C and a Cu:FeS molar ratio of 2:1 produced the lowest local Cu concentration observed by SEM–EDS area analysis. Under this condition, the analyzed metallic region contained 90.80 wt.% Fe, 7.55 wt.% P, 1.47 wt.% Cu, 0.15 wt.% S, and 0.03 wt.% Si. Increasing either the reaction temperature or the FeS addition beyond this condition did not further decrease the local Cu concentration and was accompanied by increased Cu and/or S concentrations in the analyzed metallic regions. Because these values were obtained from local SEM–EDS area analysis, they should not be interpreted as bulk compositions or used alone to determine the overall Cu-removal efficiency or Cu mass balance.

The Cu-depleted Fe–P alloy was subsequently subjected to oxidative dephosphorization. Increasing the slag basicity from 2.0 to 3.0 markedly enhanced phosphorus removal. The residual P content in the metallic phase decreased from 1.33 wt.% at a basicity of 2.0 to 0.20 wt.% at 2.5 and finally to 0.042 wt.% at 3.0. Correspondingly, the phosphorus removal efficiency increased from 86.55% to 99.44%. These results demonstrate that a higher CaO/SiO_2 ratio promoted the transfer and stabilization of oxidized phosphorus in the slag phase.

The experimental results were consistent with the thermodynamic basis of the sequential refining strategy. Cu exhibited a stronger thermodynamic affinity for sulfur than Fe, and the observed decrease in Cu concentration in the metallic phase was consistent with preferential Cu sulfidation during FeS-assisted refining. However, because the sulfide-rich phase was not directly characterized by SEM–EDS or XRD, the detailed Cu partitioning and the identity of the sulfide phases formed cannot be conclusively confirmed from the present results. In the subsequent dephosphorization stage, Fe_2O_3 provided the oxidation potential required for phosphorus oxidation, while the CaO-rich slag stabilized the oxidized phosphorus as Ca–P–O species. Thus, efficient phosphorus removal was governed by the combined effects of oxidation potential and slag chemistry.

Under the optimum dephosphorization condition at a slag basicity of 3.0, the final metallic product contained 0.042 wt.% P, 1.40 wt.% Cu, 0.004 wt.% S, and 0.006 wt.% Si, corresponding to a calculated Fe content of 98.55 wt.% based on the measured major residual impurities and an estimated Fe recovery of 93.27%. Because the Fe content was

calculated by difference rather than determined by direct total-Fe analysis, the Fe content and recovery values should be interpreted as calculated and estimated values, respectively.

Although the residual Cu concentration of the recovered Fe-rich metallic product remains higher than that typically desired for direct use in conventional steelmaking, the product may still be utilized as a secondary Fe-bearing scrap or blended feedstock. By mixing it with low-Cu scrap or virgin Fe sources at an appropriate ratio, the overall Cu concentration of the steelmaking charge can be reduced to a level suitable for the intended steel grade. Therefore, the recovered product is better regarded as a recyclable Fe-bearing secondary resource rather than a direct substitute for low-Cu steelmaking feed.

Overall, the sequential FeS-assisted sulfidation and oxidative dephosphorization route shows potential for upgrading the Fe-bearing fraction recovered from spent LFP batteries into a recyclable Fe-rich secondary metallic resource. Further work should include bulk Cu mass-balance validation, direct characterization of the sulfide-rich phase, direct total-Fe analysis, further optimization of residual Cu removal, and scale-up evaluation.

Author Contributions: Conceptualization, A.-J.I. and J.-P.W.; methodology, A.-J.I. and J.-P.W.; software, A.-J.I.; validation, A.-J.I. and J.-P.W.; formal analysis, A.-J.I.; investigation, A.-J.I.; resources, J.-P.W.; data curation, A.-J.I.; writing—original draft preparation, A.-J.I.; writing—review and editing, J.-P.W.; visualization, A.-J.I.; supervision, J.-P.W.; project administration, J.-P.W.; funding acquisition, J.-P.W. All authors have read and agreed to the published version of the manuscript.

Funding: This work was supported by the Technology Innovation Program (Development of manufacturing technology for >99.5–grade cathode raw materials (lithium compounds, NCM/NCA) by up-cycling from waste box saggar and zero emission discharge by recycling of whole by-products) (20024238) funded by the Ministry of Trade, Industry & Energy (MOTIE, Republic of Korea).

Data Availability Statement: The original contributions presented in this study are included in the article. Further inquiries can be directed to the corresponding author.

Conflicts of Interest: The authors declare no conflicts of interest.

References

1. Ralls, A.M.; Leong, K.; Clayton, J.; Fuelling, P.; Mercer, C.; Navarro, V.; Menezes, P.L. The Role of Lithium-Ion Batteries in the Growing Trend of Electric Vehicles. *Materials* **2023**, *16*, 6063. [CrossRef]
2. Waseem, M.; Lakshmi, G.; Ahmad, M.; Suhail, S. Energy Storage Technology and Its Impact in Electric Vehicle: Current Progress and Future Outlook. *Next Energy* **2025**, *6*, 100202. [CrossRef]
3. Biswal, B.K.; Zhang, B.; Tran, P.T.M.; Zhang, J.; Balasubramanian, R. Recycling of Spent Lithium-Ion Batteries for a Sustainable Future: Recent Advancements. *Chem. Soc. Rev.* **2024**, *53*, 5552–5592. [CrossRef]
4. Azimi, G.; Mohammad Zadeh, A.H. Recycling of Spent Lithium Iron Phosphate Batteries—A Review of Processes, Economics, and Carbon Footprint. *Waste Manag.* **2026**, *209*, 115203. [CrossRef]
5. Zhao, T.; Li, W.; Traversy, M.; Choi, Y.; Ghahreman, A.; Zhao, Z.; Zhang, C.; Zhao, W.; Song, Y. A Review on the Recycling of Spent Lithium Iron Phosphate Batteries. *J. Environ. Manag.* **2024**, *351*, 119670. [CrossRef]
6. Wen, G.; Yuan, S.; Dong, Z.; Ding, H.; Gao, P. Recycling of Spent Lithium Iron Phosphate Battery Cathode Materials: A Review. *J. Clean. Prod.* **2024**, *474*, 143625. [CrossRef]
7. Yao, H.; Zhang, Y.; Yang, G.; Fu, L.; Li, Y.; Zhou, L.; Geng, S.; Xiang, Y.; Seh, Z.W. Recycling of Spent Lithium Iron Phosphate Cathodes: Challenges and Progress. *ACS Appl. Mater. Interfaces* **2024**, *16*, 67087–67105. [CrossRef]
8. Ding, Y.; Fu, J.; Zhang, S.; He, X.; Zhao, B.; Ren, J.; Zhong, J.; Liu, Z. Advances in Recycling $LiFePO_4$ from Spent Lithium Batteries: A Critical Review. *Sep. Purif. Technol.* **2024**, *338*, 126551. [CrossRef]
9. Lei, S.; Sun, W.; Yang, Y. Comprehensive Technology for Recycling and Regenerating Materials from Spent Lithium Iron Phosphate Battery. *Environ. Sci. Technol.* **2024**, *58*, 3609–3628. [CrossRef]
10. Vasconcelos, D.S.; Tenório, J.A.S.; Botelho Junior, A.B.; Espinosa, D.C.R. Circular Recycling Strategies for LFP Batteries: A Review Focusing on Hydrometallurgy Sustainable Processing. *Metals* **2023**, *13*, 543. [CrossRef]
11. Yang, W.; Liu, X.; Zhou, X.; Tang, J.; Su, F.; Li, Z.; Yang, J.; Ma, Y. Mechanism of Selective Lithium Extraction from Spent $LiFePO_4$ Cathodes in Oxidizing Alkaline Leaching System. *Sep. Purif. Technol.* **2024**, *329*, 125237. [CrossRef]

12. Li, H.; Song, J.; Song, L.; Liang, J. Research on the Separation and Recovery of Iron, Lithium, and Phosphorus from Spent $LiFePO_4$ by Molten Salt Method. *Sep. Purif. Technol.* **2025**, *378*, 134749. [CrossRef]
13. Kapoor, I.; Davis, C.; Li, Z. Effect of Residual Elements during the Hot-Working Process of Steel Production: A Critical Review. *Steel Res. Int.* **2024**, *95*, 2400116. [CrossRef]
14. Zhang, Y.; Ikeda, K.; Kitsuya, S.; Miyamoto, G.; Furuhara, T. Grain Boundary Character Dependence of Phosphorus Segregation at Ferrite Grain Boundaries in a High-Purity Iron–Phosphorus Binary Alloy. *Scr. Mater.* **2024**, *249*, 116170. [CrossRef]
15. Yoon, J.-S.; Im, A.-J.; Wang, J.-P. Selective Copper Removal from an Fe–P–Cu Alloy Recovered by Pyrometallurgical Reduction of Spent $LiFePO_4$ Batteries via Sulfidation–Slag Refining. *Materials* **2026**, *19*, 1185. [CrossRef]
16. Zhang, R.; Yang, J.; Xu, L.; Wang, L.; Sun, H.; Yang, W.; Gao, J. Dephosphorization Kinetics of Hot Metal at Low Slag Basicity and Low Temperature under the Different Fe_2O_3 Addition Amounts. *Steel Res. Int.* **2024**, *95*, 2300661. [CrossRef]
17. Wang, S.; Deng, Z.; Song, G.; Zhu, M. Distribution Behaviors of Phosphorus in $CaO–SiO_2–FeO_x–MgO–MnO–Al_2O_3$ Basic Oxygen Furnace Slags. *Steel Res. Int.* **2025**, *96*, 369–379. [CrossRef]
18. Tian, S.; Cao, Y.; Dong, L.; Shi, P.; Li, R.; Jin, Y.; Tu, Y.; Du, C.; Ren, Z.; Zhou, Z. Selective Recovery of Lithium from Spent $LiFePO_4$ Powders with Electrochemical Method. *J. Environ. Chem. Eng.* **2024**, *12*, 112871. [CrossRef]

Disclaimer/Publisher's Note: The statements, opinions and data contained in all publications are solely those of the individual author(s) and contributor(s) and not of MDPI and/or the editor(s). MDPI and/or the editor(s) disclaim responsibility for any injury to people or property resulting from any ideas, methods, instructions or products referred to in the content.